Synthesis of $Ti_{1-x}W_x$ Solid Solution MAX Phases and Derived MXenes for Sodium-Ion Battery Anodes

Barak Ratzker[1,a], Bar Favelukis[1,a], Mark Baranov[2], Yugal Rathod[3,4], Avia Greenberg[1], Or Messer[1], Dor A. Goldstein[1], Alexander Upcher[2], Vladimir Ezersky[2], Nitzan Maman[2], Ido Biran[1], Varun Natu[3,4], Maxim Sokol[1,*]

[1] Department of Materials Science and Engineering, Tel Aviv University, P.O.B 39040, Ramat Aviv 6997801, Israel
[2] Ilse Katz Institute for Nanoscale Science and Technology, Ben-Gurion University of the Negev, P.O.B 653, Beer-Sheva 8410501, Israel
[3] Physical and Materials Chemistry Division, National Chemical Laboratory, Pune, 411008, India,
[4] Academy of Scientific and Innovative Research (AcSIR), Ghaziabad, Uttar Pradesh, 201002, India,

* Corresponding author: sokolmax@tauex.tau.ac.il
[a] Equal contribution

Abstract

One of the distinguishing features of MAX phases and their MXene derivatives is their remarkable chemical diversity. This diversity, coupled with the two-dimensional nature of MXenes, positions them as outstanding candidates for a wide range of electrochemical applications. In this study, we report the synthesis of M site $T_{1-x}W_x$ solid solution MAX phases, specifically $(Ti_{1-x}W_x)_2AlC$ and $(Ti_{1-x}W_x)_3AlC_2$. The 211-type phase exhibited a disordered solid solution, whereas the 312-type phase displayed a more ordered structure, resembling an *o*-MAX arrangement, with W atoms preferentially occupying the outer planes. This specific ordering in the 312-type MAX phase is attributed to the unique electronic structure and atomic radius of W, indicating that these characteristics are crucial for the preferential occupation of the outer planes.

Moreover, corresponding solid-solution MXenes, $Ti_{2.4}W_{0.6}C_2T_z$ and $Ti_{1.6}W_{0.4}CT_z$, were synthesized via selective etching of MAX powder precursors containing 20% W. These MXenes were evaluated as sodium-ion battery anodes, with $Ti_{1.6}W_{0.4}CT_z$ showing exceptional capacity, outperforming existing multilayer MXene chemistries. This work not only demonstrates the successful integration of W in meaningful quantities into a double transition metal solid solution MAX phase, but also paves the way for the development of cost-effective MXenes containing W. Such advancements significantly widen their application spectrum by fine-tuning their physical, electronic, mechanical, electrochemical, and catalytic properties.

Keywords

Tungsten, Solid-solution, MAX phases, MXenes, *o*-MAX, Sodium-ion batteries

1. Introduction

MAX phases are a diverse family of ternary atomically layered compounds that follow the formula $M_{n+1}AX_n$ [1,2]. Where n is a positive integer (typically 1 to 4), M represents an early transition metal, A represents a group-A element, typically from groups 13 and 14 of the periodic table, and X is either carbon and/or nitrogen. Owing to their layered structure and mixture of covalent, ionic, and metallic bonds, these materials exhibit a distinctive combination of physical, mechanical, and electronic properties [3–6]. Moreover, MAX phases serve as a precursor for creating MXene, a class of 2D carbides and nitrides that are synthesized by selective etching of the A layer [7,8]. MXenes are the most diverse family of 2D materials, as they can be directly derived from their parent MAX phases while preserving their inherent carbide structure and chemical composition.

MAX phases exhibit high chemical versatility and numerous quaternary (or beyond) solid solutions have been synthesized [1,2]. They can form various solid solutions in either of the M, A, or X constituents, possibly having multiple components in these respective sites. The most widespread solid solutions are double transition metal MAX phases $(M'_{1-x}M''_x)_nAX_{n-1}$ [9]. These types of MAX phase solid solutions can be either disordered or ordered. Where ordering can be out-of-plane or in-plane, termed *o*-MAX and *i*-MAX, respectively [1,10].

A prominent feature of solid solution MAX phases is that they can be used as precursors to synthesize MXenes that inherit their $M'_{1-x}M''_x$ complex structures and tunable properties. Therefore, compelling a continuous strive towards discovery of new MAX phases structures and compositions [11]. In turn, these can be used to synthesize novel MXenes [12]. As witnessed via the development of complex solid solutions and even high-entropy MXenes [13,14]. Modifying solid solution MAX and MXene by incorporating different elements enables to enhance or tune their mechanical, thermal, electronic, optical, and electrochemical properties [12,15–17]. For instance, the chemical diversity and/or disorder of solid solution MAX phases and MXenes can make them promising catalyst [18] or electrode [19–21] materials. So far, over 80 $(M'_{1-x}M''_x)_{n+1}AX_n$ disordered M site solid solutions have been synthesized [2].

Among their many potential uses, MXenes [22–25] and MXene-based composites [26–29] show promise as high-performance anode materials in sodium-ion batteries (SIBs), which are persistently sought after as a promising cost-effective alternative to lithium-ion batteries [30,31]. Moreover, tuning MXene chemistry via M site solid solutions is a promising strategy to improve electrochemical properties such as capacitance and cyclic stability of battery electrodes [17,20,32,33].

Tungsten (W) is a heavy transition metal element that offers a high valence state and strong bonding with oxygen and carbon. W-based materials are known for their electrochemical and catalytic performance [34–36]. Incorporating W into the structure of Ti-based MAX and MXenes can enable tuning of their physical and electronic properties. Possibly yielding compounds with high thermal and electrical conductivities, higher strength at elevated temperature, lower thermal expansion, and resistance to thermal shock [37]. Moreover, W-based MXenes could be promising topological insulators [38], gas sensors [39], catalysts [37,40–42], and electrodes energy storage and conversion [35,43]. For example, the implementation of other 2D W-based materials like WS_2 and WSe_2 dichalcogenides as anodes in SIBs is also considered [44,45].

To date, there are very few examples of MAX phases and even less of MXenes that contain tungsten. Meshkian et al. [37] synthesized $(W_{2/3}Sc_{1/3})_2AlC$ and $(W_{2/3}Y_{1/3})_2AlC$ *i*-MAX phases and utilized them to make $W_{1.33}C$ MXenes with vacancy ordering, which exhibited superior catalytic performance. Yang et al. [46] synthesized a variety of solid solution *i*-MAX phases comprising $(W_{2/3}R_{1/3})_2AlC$ with R being a lanthanide (Gd, Tb, Dy, Ho, Er, Tm, and Lu). Similarly, Chen et al. [47] synthesized $(W_{1/3}Mo_{1/3}R_{1/3})_2AlC$ with R being a lanthanide (Gd, Tb, Dy, Ho, Er, and Y). Notably all these W-containing MAX phases have a 211 structure and do not contain any Ti. Instead, they contained costly rare earth elements. A few other examples have been reported. Cai et al. [48] synthesized $Nb_{3.9}W_{0.1}AlC_3$ but only 2.5% of Nb was substituted by W. Similarly, Wang et al. [49] synthesized $(Ti_{1-x}W_x)_3SiC_2$ but reported that only 5 mol.% W could be incorporated into the MAX phase. Furthermore, although Si-based MAX phases serve as MXene precursors [50], it is much more convenient to have Al-based MAX phases that are easier to selectively etch. Anasori et al. [51] synthesized W-based nanolaminated carbides $(W,Ti)_4C_{4-x}$, which cannot serve as a precursor for MXenes. Up to now, disordered transition metal quaternary MAX phases that contain a considerable amount of tungsten as a second M'' element have not been realized.

In the present study we investigated the synthesis of double transition metal $Ti_{1-x}W_x$ solid solutions with 10–40% W substituting Ti in $(Ti_{1-x}W_x)_2AlC$ and $(Ti_{1-x}W_x)_3AlC_2$ structures. The phases obtained for the various compositions were analyzed and focus was given to the characterization of Ti–20%W MAX phases and their corresponding MXenes. Furthermore, the potential application of W-containing solid solution MXenes as SIB anodes was assessed.

2. Experimental

2.1 MAX phases synthesis

The starting powders used to synthesize the MAX phases were Ti (99.5%, ~45 µm, Eckart), W (99.9%, 1–5 µm, Alfa Aesar), Al (99.5%, ~325 mesh, Thermo Scientific), TiC (99.5%, ~ 2 µm, Thermo Scientific), and C (99%, ~325 mesh, Thermo Scientific). The powder mixtures were prepared in a tumbler mixer according to molar ratios to obtain targeted $(Ti_{1-x}W_{x)2}AlC$ and $(Ti_{1-x}W_x)_3AlC_2$ MAX phases, where x=0, 0.1, 0.2, 0.3, and 0.4. For example, to yield solid solutions of $Ti_{1.6}W_{0.4}AlC$ (211) and $Ti_{2.4}W_{0.6}AlC_2$ (312) powders of Ti:W:Al:TiC were mixed at ratios of 0.6:0.4:1.05:1 and 0.4:0.6:1.05:2, respectively. In all samples Al was added in 5% excess of the desired stoichiometry. The detailed powder mixtures compositions and targeted stoichiometries can be found in the Supplementary Information (SI) Table S1. 5 g of each powder mixture were cold compacted into circular pellets with a diameter of 20 mm under uniaxial pressure of ~45 MPa. The resulting green bodies were placed in an alumina crucible and inserted into an 80 mm tube furnace (TMAX-Threefurnace2). The high-temperature synthesis was carried out at 1450°C for 3 h under a protective atmosphere using Ar/5%H_2 at a flow rate of 100 sccm. The heating and cooling rate was 5 °C/min. After synthesis the samples were drilled and ground to a powder. The MAX phases used as MXene precursors were sieved to obtain powders with a particle size ≤ 20 µm.

2.2 MXene synthesis

The produced $Ti_{1.6}W_{0.4}AlC$ and $Ti_{2.4}W_{0.6}AlC_2$ were selected as precursors for MXene synthesis. The corresponding $Ti_{1.6}W_{0.4}CT_z$ and $Ti_{2.4}W_{0.6}C_2T_z$ were synthesized by selectively etching the Al layer from the MAX phase precursors. For each, 1 g of MAX phase powder was etched in a 20 ml mixture of HCl, HF, and DI water for 72 h at 45°C; using a ratio of 12:4:4 and for 12:2:6 for $Ti_{1.6}W_{0.4}CT_z$ and $Ti_{2.4}W_{0.6}C_2T_z$, respectively. The etched MAX powders were centrifuged at 3500 RPM in DI water until the pH reached 6. It was then mixed with a 20 ml 5 wt% tetramethylammonium hydroxide (TMAOH; 98%, Thermo Scientific) solution and stirred for 3 h with N_2 bubbling. The intercalated MXene mixture was centrifuged again with ethanol and DI water several times, then sonicated for 1 h and centrifuged for 1 h to separate the MXene colloidal solution from the multilayer sediment. Free-standing films were prepared by pouring 5 ml of each MXene colloidal solution into a vacuum filtering system equipped with a Celgard 3105 separator.

2.3 Characterization

2.3.1 Phase analysis

X-ray diffraction (XRD) analysis was carried out on all the synthesized powders. Powder samples were mounted on an amorphous silicon holder for data collection at room temperature using a PANalytical AERIS X-ray diffractometer with a standard Cu $K\alpha$ x-ray radiation source (λ = 1.5406 Å). A total of 7178 points were collected within a 2θ ranges of 7°-85° with a step size of 0.01086° and scan speed of 0.0557 °/sec. Unit cell dimensions, space group assignment, data reduction and finalization were done by using the GSAS software package [52] (ver. 5711, released 2024). The background fitting was done using a Chebyschev function. The structures were solved in the hexagonal $P6_3/mmc$ space group (no. 194) and refined through the Rietveld refinement method using a full-matrix least-squares technique, using pseudo-Voight type peak profile functions. Graphics were done by the Olex2 software package [53]. The final refinement cycle included the atomic, instrumental, and sample parameters.

2.3.2 Electron microscopy

The MAX powder particles obtained for Ti–20%W were examined by high resolution scanning electron microscopy (HRSEM) (ZEISS Gemini 300). Ti–20%W multilayered and single flake MXenes were drop cast on transmission electron microscope (TEM) copper grids of continuous (Type B) or ultra-thin carbon film on lacy carbon support, respectively. Both kinds of multilayer and single flake MXenes were examined by the same HRSEM operating at 30 kV using a scanning transmission electron microscopy (STEM) detector. The cross-section of the free-standing MXene films were examined by SEM (JEOL JSM-IT200). Thin lamellae for TEM examination were prepared from MAX phase particles by focused ion beam (FIB) (FEI Helios G4 UC). Atomic scale characterization of the MAX and MXenes, deposited on the aforementioned TEM grids, was carried out by high resolution STEM, using a Cs-corrected (S-CORR) probe operating at 200 kV (Thermo Fisher Scientific Spectra 200). The images were recorded in STEM mode with high angle annular dark field (HAADF) detector. Energy dispersive x-ray spectroscopy (EDS) spectra were collected with a Super-X (Thermo Fisher Scientific) silicon drift detector (SDD). The images and the EDS spectra were processed with Thermo Fisher Scientific Velox software (version 3.10).

2.3.3 Spectroscopy measurements of MXene

Diluted colloidal solutions containing approximately 0.05 g/ml single flake MXenes in DI water were prepared inside quartz cuvettes and the UV–vis–NIR absorption spectra between 200–900 nm wavelength were measured in transmission mode using a spectrophotometer

(Shimadzu UV-2600). XRD examination of the MXene free-standing films was performed using the same system described above. X-ray photoelectron spectroscopy (XPS) was performed on the free-standing MXene films using an ESCALAB QXi system (Thermo Scientific, USA). High resolution spectra were collected with a pass energy of 20 eV.

2.3.4 Electrochemical measurements and SIB anode performance

First electrodes were prepared. The MXene was mixed with carbon black (99%, Alfa Aesar) and polyvinylidene fluoride (PVDF) in a ratio of 80:10:10 respectively. Then N-Methyl-2-pyrrolidone (NMP) was added to make a slurry, which was cast on an Al foil using a doctor blade. After vacuum drying electrodes were punched out and 2032 coin cells were assembled inside an Ar filled glovebox. Celgard separators were used, and Na-ion metal was used as counter electrode. Two different electrolyte solvents were tested; diglyme (DG) and a 1:1 mixture of ethylene carbonate : dimethyl carbonate (EC:DMC) with 5% fluoroethylene carbonate (FEC) (carbonate) with 1M $NaPF_6$ dissolved in it. The performance of as assembled cells was tested assessed by a Neware BTS4000 battery tester.

3. Results and discussion

3.1 Effect of varying tungsten content on MAX synthesis products

The phase compositions following synthesis of $(Ti_{1-x}W_x)_2AlC$ and $(Ti_{1-x}W_x)_3AlC_2$ with varying W content (x=0, 0.1, 0.2, 0.3, 0.4) were determined by XRD (Figure 1). The phase fractions weight percentages were determined by Rietveld refinement. For an addition of 10% W, nearly pure $Ti_{1.8}W_{0.2}AlC$ (211 MAX) and pure $Ti_{2.7}W_{0.3}AlC_2$ (312 MAX) were obtained, with a small trace of $(Ti_{1-x}W_x)_3AlC_2$ (1.6 wt.%) in the 211 phase and TiC (1.2 wt.%) in the 312 phase. Similarly, for the addition of 20% W nearly pure $Ti_{1.6}W_{0.4}AlC$ or $Ti_{2.4}W_{0.6}AlC_2$ were obtained, with only a negligible trace of 312 MAX (2.0 wt.%) or W (0.7 wt.%), respectively. In stark contrast to the purity of the MAX phases obtained at 10-20% W, addition of 30% and 40% W to the reaction led to significant amounts of various other phases, including different MAX phases, metal carbides, intermetallic and residual metals. Additionally, trace amounts of unidentified phases appeared and did not have sufficiently high intensity to be properly identified.

For the targeted 211 $(Ti_{1-x}W_x)_2AlC$ stoichiometry, addition of 30% W led to formation of a 312 MAX phase ($Ti_{2.6}W_{0.4}AlC_2$, 27.6 wt.%) alongside the desired 211 MAX phase ($Ti_{1.4}W_{0.6}AlC$, 58.7 wt.%). Interestingly, a novel rhombohedral (*R3m*) intermetallic phase,

$Ti_{17.6}W_{8.4}$, was observed (10.3 wt.%), structurally analogous to the rhombohedral distorted γ-phase like Au_5Zn_8 [54] (Figure S13). Furthermore, more metallic W (3.4 wt.%) was detected. Addition of 40% W resulted in a complete absence of a 211 MAX phase, instead showcasing a 312 MAX phase ($Ti_{2.1}W_{0.9}AlC_2$, 70.5 wt.%) alongside abundant $Ti_{17.6}W_{8.4}$ (11.9 wt.%), metallic W (17.6 wt.%). Naturally all the synthesized 211 MAX phase solid solutions exhibit a single unique Wycoff position (Figure S3) that is shared between the W and Ti atoms (with partial occupancies). Leading to an equimolar disorder throughout the structure, with the W:Ti distribution changing in a linear fashion, that is, $W_{0.1}$:$Ti_{0.9}$, $W_{0.2}$:$Ti_{0.8}$, and $W_{0.3}$:$Ti_{0.7}$ for the 211 MAX $(Ti_{1-x}W_x)_2AlC$ (x = 0.1, 0.2, 0.3) phases, respectively.

In the case of the targeted 312 $(Ti_{1-x}W_x)_3AlC_2$ stoichiometry, it becomes increasingly apparent with rising W content that the MAX phases tend to exhibit out-of-plane ordering (Table S5). In contrast to the 211 phases, the unit cells of the 312 phases contain two unique Wycoff positions. One relating to the outer planes – *4f*, with M in closer proximity to A, and the other relating to the inner "sandwiched" plane of M – *2a*. Examination of these unique positions makes it clear that the substitution of Ti by W primarily occurs at the outer planes, as indicated by the refinement of partial occupancies (Figures S5-8 and Table S5). This seems to be in line with the first principal calculations conducted by Dahlquist and Rosen [55]. Suggesting that under the synthesis conditions used herein, T = 1723 K, the observed disorder in the *2a* and *4f* positions results in $\Delta H < 0$ for solid solutions containing W in a TiM_2AlC_2 system. It is worth noting that other group VI transition elements (i.e., Cr and Mo) readily form *o*-MAX structures, as is the case of $(Cr_{0.5}V_{0.5})_{n+1}AlC_n$ [56] or $(Ta_{1-x}Ti_x)_3AlC_2$ [57]. Thus, in these cases, the MAX phase solid solutions exhibit ordering tendencies towards the *4f* position alone. This well-defined preferential exchange at the outer planes is perceivable by the gradual change in the basal peak intensity ratios for the solid solution $(Ti_{1-x}W_x)_3AlC_2$ phases compared to Ti_3AlC_2, whereby the intensities of the (0002) and (0004) reflections diminish and grow, at 2θ = 8° and 2θ = 17°, respectively, as seen in Figure 1a for the 312 MAX phases.

Comprehensive lists of the synthesis targeted compositions, resulting phases by weight percentage, and Rietveld analysis of the X-ray diffraction (XRD) spectra are detailed in SI Figures S1-S8 and Tables S2-S9. The crystal structure diagrams of the solid solution MAX and *o*-MAX phases are shown in SI Figures S9-S12. The analysis confirms the hexagonal space group $P6_3/mmc$ for both the 211 and 312 MAX phase solid solutions, with some important distinctions regarding internal composition.

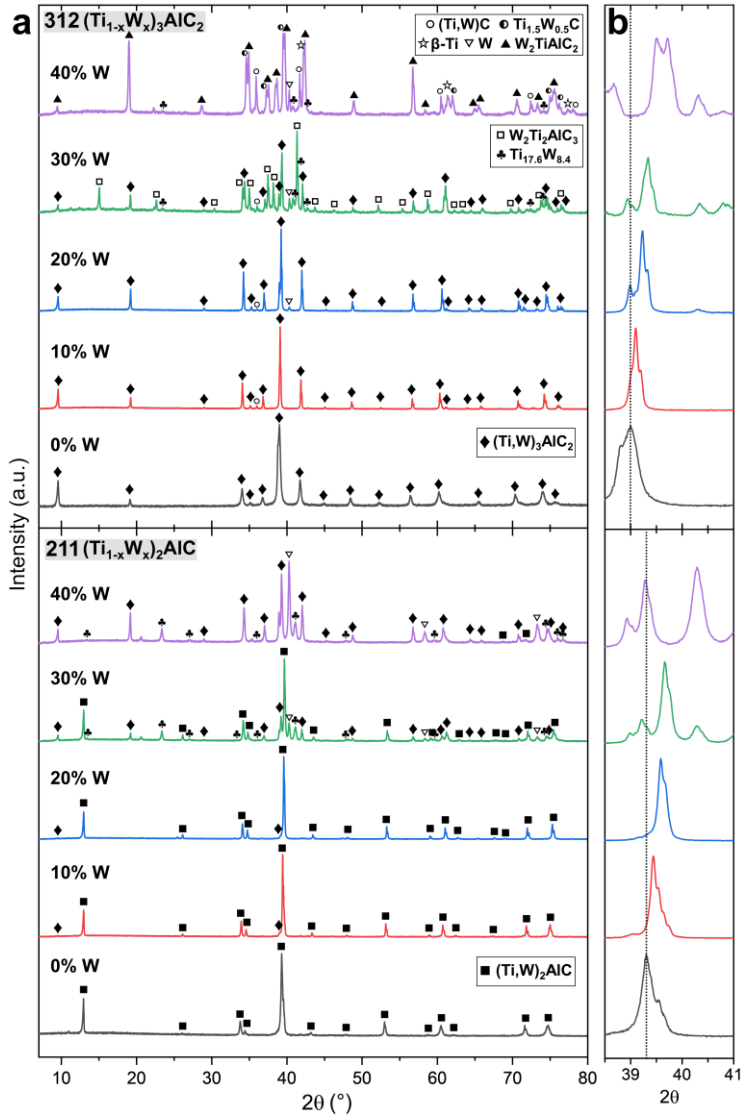

Figure 1. XRD analysis. (a) XRD patterns of synthesized powders aimed at solid solution MAX phases $(Ti_{1-x}W_x)_2AlC$ and $(Ti_{1-x}W_x)_3AlC_2$ with varying W content (x=0, 0.1, 0.2, 0.3, 0.4). (b) Zoom-in on the high intensity peak around 39-40° 2θ, indicating a shrinkage in the lattice parameter. Crystal data on the detected phases can be found in the SI (Figures S1-S13 and Tables S2-S9).

Table 1. Fraction of phases (wt.%) in each sample as determined by Rietveld refinement.

MAX-W%	$Ti_{2-x}W_xAlC$ (211)	$Ti_{2-x}W_xAlC_2$ (312)	$Ti_2W_2AlC_3$ (413)	$Ti_{17.6}W_{8.4}$	W	$Ti_{1.5}W_{0.5}C$	TiC	*β*-Ti
211 – 10%	98.4	1.6	---	---	---	---	---	---
211 – 20%	98.0	2.0	---	---	---	---	---	---
211 – 30%	58.7	27.6	---	10.3	3.4	---	---	---
211 – 40%	---	70.5	---	11.9	17.6	---	---	---
312 – 10%	---	98.8	---	---	---	---	1.2	---
312 – 20%	---	97.1	---	---	0.7	---	2.2	---
312 – 30%	---	42.4	48.1	5.3	1.4	---	2.8	---
312 – 40%	---	60.4 (*o*-MAX)	---	---	2.2	7.6	24.3	5.5

3.2 Crystallographic analysis

Analysis of the refinement results shows that for the 10% W addition the *4f* position exhibits a $W_{0.14}$:$Ti_{0.86}$ distribution, while the *2a* inner W/Ti position results in a $W_{0.02}$:$Ti_{0.98}$ distribution. Progressing in a linear fashion, the 20% W addition exhibits a $W_{0.28}$:$Ti_{0.72}$ and $W_{0.04}$:$Ti_{0.96}$ distribution in the *4f* and *2a* positions, respectively. However, addition of 30% W led to a mixture of products, with two predominant ordered MAX phases: (1) a 413 MAX phase $W_2T_2AlC_3$ (48.1 wt.%) analogous to $M''_2M'_2AlC_3$ [58] *o*-MAX structures (Figure S12). Containing two distinct Wycoff positions, one relating to the outer planes, *4e*, with a $W_{0.8}$:$Ti_{0.2}$ distribution, and the second relating to the inner planes, *4f*, with a $W_{0.2}$:$Ti_{0.8}$ distribution. (2) The target 312 MAX phase, $Ti_{2.1}W_{0.9}AlC_2$ (42.4 wt.%). However, with a W:Ti distribution that deviated from the linear trend observed for the 10-20% W additions (similar to the 211 MAX phases). In this case, it encompassed a much more significant exchange of the Ti by W in the inner layer, resulting in a $W_{0.14}$:$Ti_{0.86}$ and $W_{0.38}$:$Ti_{0.62}$ distribution in the *2a* and *4f* positions respectively. Had the exchange been linear with previous stoichiometries the distribution in the *2a* position would be $W_{0.06}$:$Ti_{0.94}$. In addition, small amounts of the intermetallic $Ti_{17.6}W_{8.4}$ (5.3 wt.%) phase and W metal (1.4 wt.%) and TiC (2.8 wt.%) were observed. Finally, the most diverse structural array was obtained by adding 40% W to the targeted 312 stoichiometry. In this case, the main phase obtained was W_2TiAlC_2 (60.4 wt.%), which is analogous to other *o*-MAX structures of the $M''_2M'AlC_2$ family [59]. It exhibited W:Ti distributions of $W_{0.2}$:$Ti_{0.8}$ and $W_{0.9}$:$Ti_{0.1}$ in the *2a* and *4f* positions, respectively. The remaining phases observed in the mixture were TiC (24.3 wt.%), $Ti_{1.5}W_{0.5}C$ (7.6 wt.%), *β*-Ti (5.5 wt.%) – a high-temperature Ti polymorph, and W (2.2 wt.%).

As noted, smaller fractions of W are localized in the central layer in the obtained 312 MAX solid solutions. A feature that indicates W atoms behave more similarly to Cr rather than Mo, which typically exists only in the outer *o*-MAX layers [60]. It is anticipated that the overall lattice will shrink since the atomic radius of W (135 pm) is slightly smaller than that of Ti (140 pm) [61]. This is plainly observed by the shift to higher 2θ° angles with W content in both types of MAX phases, as shown for the high intensity peaks (Figure 1b). In both $(Ti_{1-x}W_x)_2AlC$ and $(Ti_{1-x}W_x)_3AlC_2$ the *a* lattice parameter decreased linearly with the increasing amount of W (0-30%), from 3.056 to 3.025 Å and 3.073 to 3.043 Å in the 211 and 312 phases, respectively (Figure 2a). Moreover, it further shrunk down to 3.001 Å in the 312 W_2TiAlC *o*-MAX phase (Table S4), seemingly obeying Vegard's law within the Ti/W carbide region. However, in contrast to the *a* lattice parameter, the *c* lattice parameter displayed an abnormal behavior. Particularly pronounced in the 312-type structure (Figure 2b), as compared to the parent

Ti_3AlC_2 phase. Initially, there was a decrease from 18.581 to 18.461 Å at 10% W for $Ti_{2.7}W_{0.3}AlC_2$, followed by a further decrease to 18.445 Å at 20% W for $Ti_{2.4}W_{0.6}AlC_2$. Subsequently, there was an *increase* to 18.497 Å at 30% W for $Ti_{2.1}W_{0.9}AlC_2$, and finally to *c* = 18.689 Å for the W_2TiAlC *o*-MAX phase, obtained at 40% W. Even surpassing the *c*/*a* ratio of the parent Ti_3AlC_2-type structure. This behavior contrasts with other reports on M site solid solutions, where both *a* and *c* concurrently decrease or increase depending on the substituting element [15,62,63]. The abrupt increase in *c* when increasing the W content from 20 to 30% is attributed to the non-linear exchange of Ti atoms by W in the inner M layer at the *2a* position.

Thus, the inclination towards out-of-plane ordering for the 312 structure alters the crystal unit cell so that the *c*/*a* ratio changes irregularly (Figure 2c) when accommodating W in a non-linear fashion in the two distinct Wycoff positions. In contrast, as the 211 structure is limited to exchange of Ti by W in a single Wycoff position, the *c*/*a* ratio increases linearly. Notwithstanding, when considering the slightly smaller atomic radius of W compared to that of Ti, arising from the lanthanide contraction phenomenon [64], the overall unit cell volume of the phases in both the cases follows a definitive downward trend (Figure 2d). Decreasing from 110.18 to 107.98 $Å^3$ and 151.96 to 148.35 $Å^3$ for the 211 and 312 MAX phases, respectively. As expected, the volume of the W_2TiAlC *o*-MAX phase decreased even further to 145.81 $Å^3$.

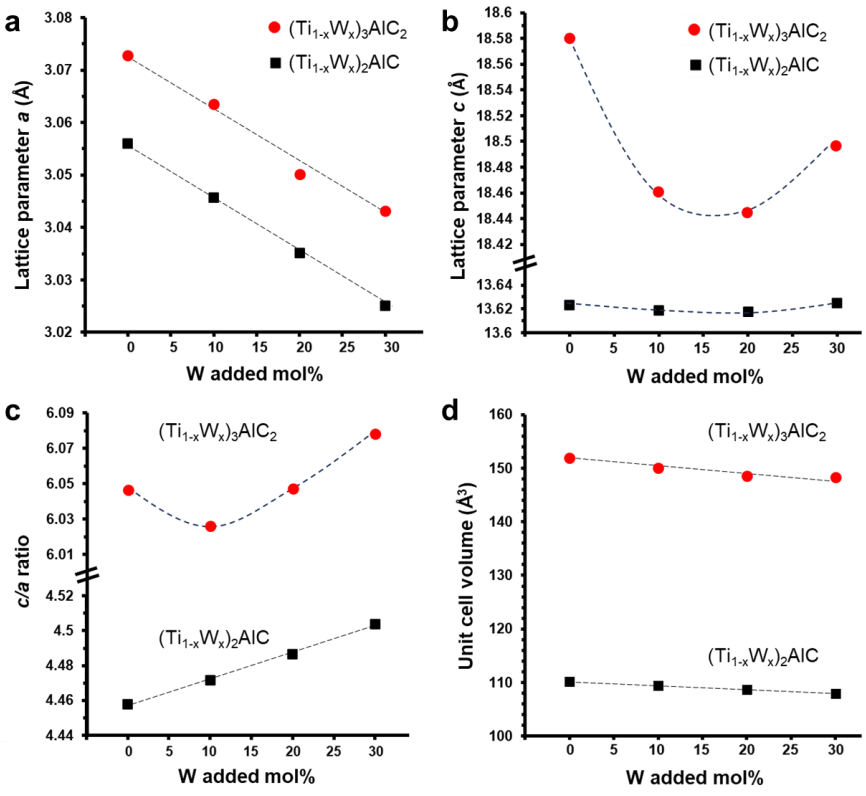

Figure 2. The change in (a) *a* and (b) *c* lattice parameters, (c) *c*/*a* ratios, and (d) unit cell volume of $(Ti_{1-x}W_x)_2AlC$ and $(Ti_{1-x}W_x)_3AlC_2$ with addition of between 0 to 30% W (x=0, 0.1, 0.2, 0.3).

A more fundamental insight to the MAX structure change can be gained when considering the bond lengths of the *4f* and *2a* positions containing W/Ti in relation to the C and Al atomic layers situated between them. The atomic positions of the *4f* W/Ti and C, also having a *4f* position (Figure 3a), were refined. During refinement the *4f* positions that are located within the unit cell could move freely along the z direction (coordinates [1/3, 2/3, z] for W/Ti, [2/3, 1/3, z] for C). Showing a linear decrease in the *4f* W/Ti–C average bond length (Figure 3b) with increased content of W, from 214 to 208 pm. While the *2a* position, located on the edge of the unit cell (coordinates 0, 0, 0), shows an increase in the average *2a* W/Ti–C bond length with a quadratic dependency (Figure 3c), from 214 to 225 pm. The average *4f* W/Ti–Al bond length also features a linear decrease, from 288 to 277 pm (Figure 3d), as do the Al–Al bond lengths, from 307 pm to 304 pm, which are tied to the linear decrease in the *a* unit cell parameter.

The higher electronegativity associated with the W atoms [55] necessitates compensation in the chemical composition of the disordered *4f* and *2a* sites in $Ti_{2.1}W_{0.9}AlC_2$. This leads to the large non-linear increase in W content at the *2a* position for the addition of 30% W. As the bond length of W/Ti-C in this position, 225 pm, surpasses even that of pure tungsten carbide, 220 pm [65]. In turn causing considerable weakening of the inner layer W/Ti-C bond and facilitating the formation of the various phases observed in the solid mixture. It is worth noting that for the *o*-MAX phase, W_2TiAlC_2, the bond length between the *2a* and *4f* positions of W/Ti and C is relaxed to bond lengths of 214 and 215 pm, respectively, which is similar to that of the parent Ti_3AlC_2. This relaxation is consistent with a local minimum of energy observed for another group VI substituted 312 MAX phase, Cr_2TiAlC_2, investigated by Burr et al. [66].

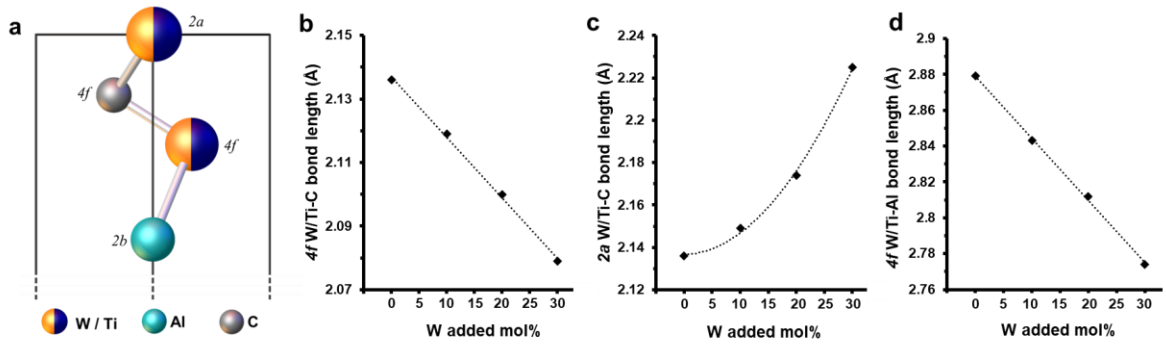

Figure 3. Changes in bond lengths for the $(Ti_{1-x}W_x)_3AlC_2$ phases with 0-30% W added. (a) Wycoff positions of the atoms comprising the asymmetric unit within the unit cell. (b) Linear decrease in the *4f* W/Ti-C bond length, (c) quadratic increase in the *2a* W/Ti-C bond length, and (d) linear decrease in the *4f* W/Ti-Al bond length.

3.3 MAX phases microstructure analysis

The $Ti_{1.6}W_{0.4}AlC$ and $Ti_{2.4}W_{0.6}AlC_2$ solid solution MAX phases with 20% W were selected as the MXene precursors. A choice based on the synthesis products having high purity, 98 and 97 % for the 211 and 312, respectively, and containing a significant amount of W. The analyzed crystal structure of the $Ti_{1.6}W_{0.4}AlC$ (211) and $Ti_{2.4}W_{0.6}AlC_2$ (312) phases are shown in Figure 3a-b. As mentioned above, the crystalline lattice of $Ti_{1.6}W_{0.4}AlC$ exhibits disorder within a single Wycoff position with a mixture ratio of $Ti_{0.8}$:$W_{0.2}$, while for $Ti_{2.4}W_{0.6}AlC_2$, the crystalline lattice exhibits disorder within two distinct Wycoff positions, *2a* and *4f*, showing mixtures of $Ti_{0.96}$:$W_{0.04}$ and $Ti_{0.72}$:$W_{0.28}$, respectively.

Table 2. Wyckoff positions and occupancies within the unit cell of $Ti_{1.6}W_{0.4}AlC$ and $Ti_{2.4}W_{0.6}AlC_2$.

Phase	Atom designation (type)	Wyckoff position (coordinates)	Occupancy
$Ti_{1.6}W_{0.4}AlC$	Ti1 (Ti)	4f (1/3, 2/3, 0.08592)	0.8
	W1 (W)	4f (1/3, 2/3, 0.08592)	0.2
	Al1 (Al)	2c (2/3, 1/3, 1/4)	1
	C1 (C)	2a (0, 0, 0)	1
$Ti_{2.4}W_{0.6}AlC_2$	Ti1 (Ti)	2a (0, 0, 0)	0.96
	W1 (W)	2a (0, 0, 0)	0.04
	Ti2 (Ti)	4f (1/3, 2/3, 0.13113)	0.72
	W2 (W)	4f (1/3, 2/3, 0.13113)	0.28
	Al1 (Al)	2b (0, 0, 1/4)	1
	C1 (C)	4f (2/3, 1/3, 0.06707)	1

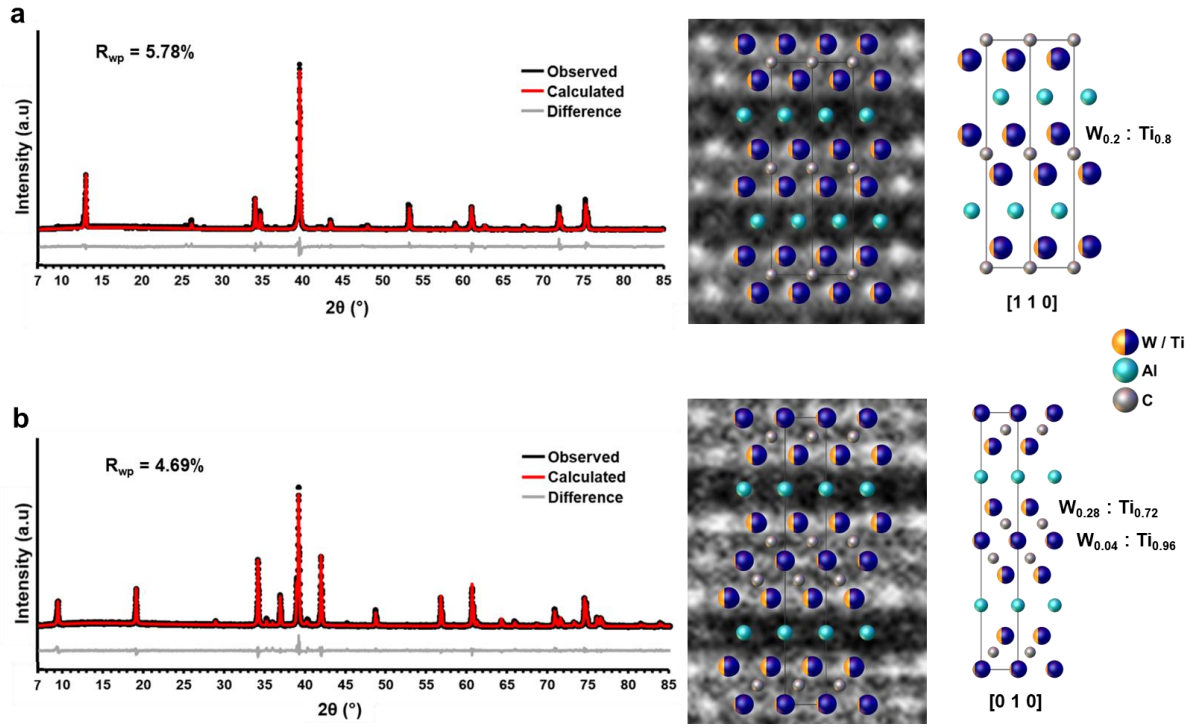

Figure 3. Crystal structure analysis of Ti–20%W MAX phase solid solutions of (a) $Ti_{1.6}W_{0.4}AlC$ and (b) $Ti_{2.4}W_{0.6}AlC_2$. Left: the results of the Rietveld refinement, confirming the hexagonal space group *P6₃/mmc* for both phases. Right: HAADF images overlayed with and alongside the corresponding unit cell crystal structure viewed along [110] and [010] directions for $Ti_{1.6}W_{0.4}AlC$ and $Ti_{2.4}W_{0.6}AlC_2$, respectively.

Examination of the $Ti_{1.6}W_{0.4}AlC$ and $Ti_{2.4}W_{0.6}AlC_2$ solid solution MAX phases microstructure was conducted (Figure 4). The powder particles exhibited a typical MAX phase faceted morphology with obvious layers and kinks (Figure 4a,d). The distinct atomic layering was observed by high resolution STEM from the viewing direction of [110] and [010] zone axis in the case of $Ti_{1.6}W_{0.4}AlC$ (Figure 4b) and $Ti_{2.4}W_{0.6}AlC_2$ (Figure 4e), respectively. For the $Ti_{2.4}W_{0.6}AlC_2$ there is a noticeable difference with the HAADF contrast between the inner and outer layers of the Ti-W carbide. As shown clearly by the overlayed integrated HAADF intensity line profile (Figure 4e and Figure S14). The higher intensity in the outer layers clearly reflects the preference of W atoms to occupy the *4f* position at the outer layers. Depletion of Ti and enrichment of W in the outer layers was confirmed by EDS, showing correlative periodic intensities of Ti and W (Figure 4f). This illustrates the inclination of Ti-W solid solutions towards forming an *o*-MAX structure. This preference is also evident in the SAED pattern (Figure 4e insert), as in the XRD patterns (Figure 1a).

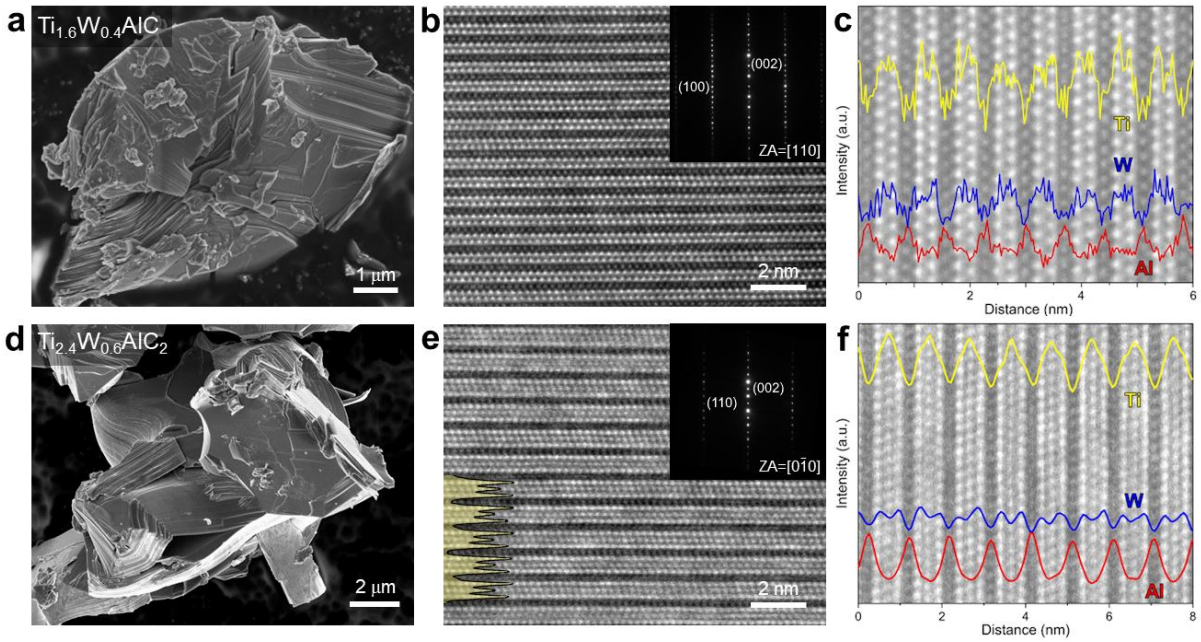

Figure 4. Microstructural and atomic scale characterization of Ti–20%W solid solution MAX phases (a-c) 211 structure $Ti_{1.6}W_{0.4}AlC$ and (d-f) 312 structure $Ti_{2.4}W_{0.6}AlC$. (a,d) HRSEM of MAX phase particles. (b,c) high resolution STEM showing the atomic structure viewed along zone axis (b) [110] and (e) [010] of $Ti_{1.6}W_{0.4}AlC$ and $Ti_{2.4}W_{0.6}AlC$, respectively. Integrated intensity is overlayed on the bottom left, a larger depiction can be found in Figure S14. (c,f) EDS compositional line profiles obtained from elemental mapping of Ti (yellow), W (blue), and Al (red) overlaying the corresponding atomically layered structure.

3.4 MXene synthesis and microstructural characterization

Synthesis of MXenes from the Ti–20%W phase solid solution precursors could not be realized by usual methods used for pure Ti-based MAX. More aggressive etching was required, and intercalation was not achieved using common intercalants like LiF/LiCl. Both types of MXenes, $Ti_{2.4}W_{0.6}C_2T_z$ and $Ti_{1.6}W_{0.4}CT_z$, required relatively longer etch times using HCl/5%HF and HCl/10%HF, respectively, and intercalation by TMAOH. The use of organic bases for intercalation makes it easier to exfoliate the MXene and alters the surface chemistry replacing –F terminations with –O and –OH [67]. Other reports also show that aggressive etching/intercalation approaches are required for obtaining solid solution [12] or Mo-based MXenes [68], indicating modified chemical response of the parent solid solution MAX phase related to differences in the chemical bonding.

The microstructural features of both kinds of obtained MXenes were examined (Figure 5). Etched multilayer MXenes of both kinds had typical morphology (Figure 4a,e). The 2D atomically layered carbide structure was consistent with that of the MAX phase precursors (Figure 5b,f). The $Ti_{2.4}W_{0.6}C_2T_z$ displayed the same *o*-MAX inclined ordering, evident by the higher intensity of the outer layers when imaged by high-resolution STEM HAADF (Figure

S15). Slight oxidation in the form of very fine nanoparticles can be observed. The single flake $Ti_{1.6}W_{0.4}CT_z$ appears to be more oxidized compared to the $Ti_{2.4}W_{0.6}C_2T_z$, corroborating the XPS results. High resolution STEM imaging of single flakes (Figure 4d,h) shows the presence of heavy W atoms appearing very bright in HAADF contrast. In both kinds of MXenes a disordered distribution of the W is observed when viewed from the [001] basal plane direction. Lower magnification micrographs showing the homogenous distribution of the W atoms are shown in SI Figure S16. Both types of MXenes are also slightly perforated (Figure 4c,g) and contain vacancies (Figure 4d,h), which is probably a result of over-etching [69]. The presence of oxidation and perforations warrants further optimization of the synthesis process of these solid solution MXenes. It should be emphasized that herein we provide an alternative way to obtain W-containing MXenes, albeit in a solid solution with Ti, without requiring to etch away costly rare-earth elements in the MAX phase precursors [37].

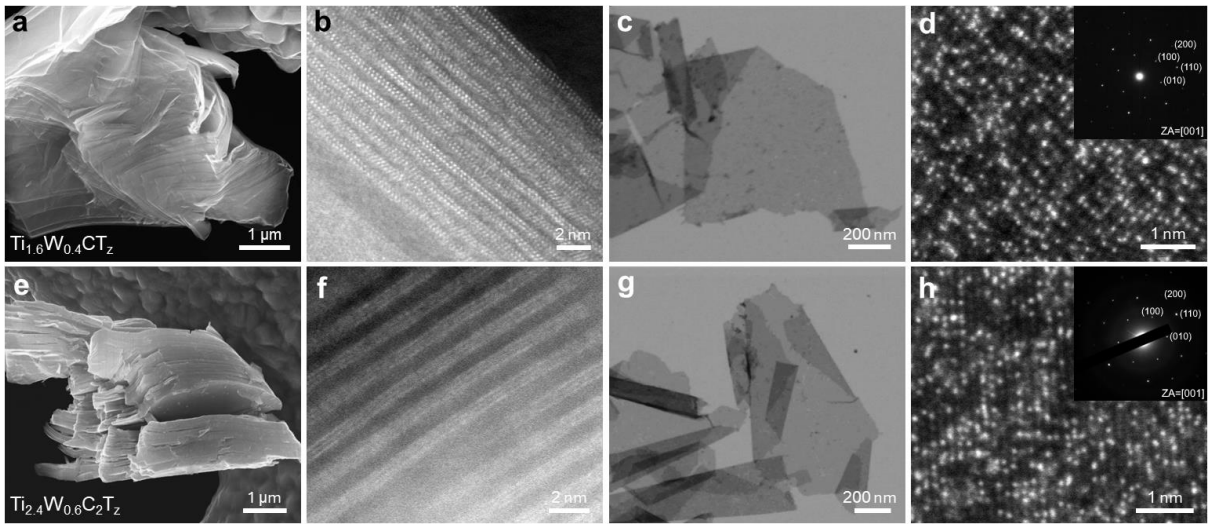

Figure 5. Microstructural and atomic scale characterization of solid-solution MXenes (a-d) $Ti_{1.6}W_{0.4}CT_z$ (e-h) $Ti_{2.4}W_{0.6}C_2T_z$. (a,e) HRSEM micrographs using a STEM detector and (b,f) TEM HAADF high resolution STEM of multilayered MXenes. (c,g) HRSEM micrographs using a STEM detector and (d,h) TEM HAADF high resolution STEM of single flake MXenes as viewed from the [001] direction. The corresponding SAED patterns are inserted in (d) and (h), respectively.

3.5 MXene optical, structural, and chemical properties

The solid solution $Ti_{2.4}W_{0.6}C_2T_z$ and $Ti_{1.6}W_{0.4}CT_z$ MXenes exhibit altered optical properties with respect to their pure Ti_2CT_z and $Ti_3C_2T_z$ counterparts. Seen in their colloid absorption spectrum and the color of colloidal solution and dry films (Figure 6a-b). Compared to regular Ti-based MXenes the Ti–20%W solid solutions colloids exhibit a noticeable blueshift in their surface plasmon resonance absorption peaks [70]. The $Ti_{2.4}W_{0.6}C_2T_z$ absorbance peak shifts to ~565 nm compared to ~582 nm for $Ti_3C_2T_z$ and the $Ti_{1.6}W_{0.4}CT_z$ exhibits absorption peaks at

~385 and ~635 nm compared to ~406 and ~900 nm observed for Ti_2CT_z. Note that the blueshift is very substantial in the NIR absorption peak shifting into visible wavelengths for the $Ti_{1.6}W_{0.4}CT_z$. When comparing the absorbance of $Ti_{1.6}W_{0.4}CT_z$ to other $M'_{1-x}M''_xCT_z$ transition metal solid-solution systems comprising Ti with 20% Nb or V the effect of W shows closer resemblance to that of $Ti_{1.6}Nb_{0.4}CT_z$ [12]. The color of the different colloids was not very different with the $Ti_{1.6}W_{0.4}CT_z$ being more greenish and $Ti_{2.4}W_{0.6}C_2T_z$ brownish (Figure 6a insert). However, there was a noticeable difference in the color of their corresponding free-standing films (Figure 5b insert). These colors are highly sensitive to the structure and composition of the MXenes [70].

The XRD spectra of the free-standing $Ti_{1.6}W_{0.4}CT_z$ and $Ti_{2.4}W_{0.6}C_2T_z$ films (Figure 5b) confirm the basal plane alignment and M_2XT_z and $M_3X_2T_z$ 2D carbide crystal structure [71], respectively. Moreover, it reflects the purity of the MXene in that there are no other crystalline phases present. The XPS spectra for Ti2p and W4f for both kinds of MXenes (Figure 6c) reveal the chemical state of the surface Ti and W atoms. It is evident that the $Ti_{1.6}W_{0.4}CT_z$ MXene is more oxidized than $Ti_{2.4}W_{0.6}C_2T_z$. Also reflected in the high brittleness of the $Ti_{1.6}W_{0.4}CT_z$ film compared to $Ti_{2.4}W_{0.6}C_2T_z$, as can be seen in the SEM micrographs inserted in Figure 6b. This is not surprising given the much higher oxidation susceptibility of M_2XT_z compared to $M_3X_2T_z$ MXenes [72,73]. Furthermore, the XPS results suggest a stronger inclination of Ti over W, although it has been shown that substitution of Ti with another transition element like Ta can improve electrochemical oxidation resistance in $(Ti_{0.95}Ta_{0.05})_3C_2T_z$ [74].

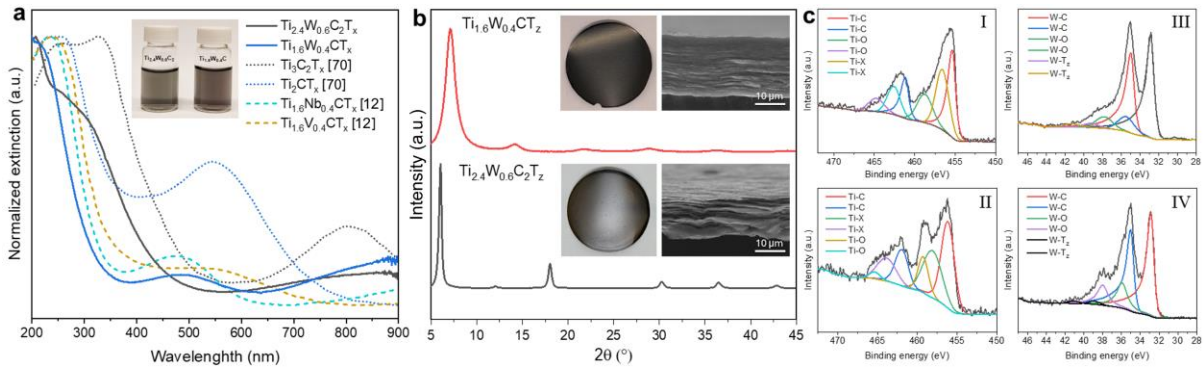

Figure 6. Spectroscopic characterization of solid solution $Ti_{2.4}W_{0.6}C_2T_z$ and $Ti_{1.6}W_{0.4}CT_z$ MXenes. (a) UV–Vis–NIR spectra absorption spectra compared to literature data of regular Ti_3CT_z and $Ti_3C_2T_z$ MXenes [70] and other transition metal solid solution $M'_{1-x}M_x''CT_z$ MXenes with either 20% Nb or V mixed with Ti in the form of $Ti_{1.6}Nb_{0.4}CT_z$ and $Ti_{1.6}V_{0.4}CT_z$ [12]. A photograph of the colloidal solutions in DI water is inserted. (b) XRD spectra of free-standing films created from $Ti_{2.4}W_{0.6}C_2T_z$ and $Ti_{1.6}W_{0.4}CT_z$, the appearance of the films and their cross section observed by SEM are inserted. (c) XPS spectra of (I-II) Ti2p and (III-IV) W4f binding energies obtained from the surface of the $Ti_{2.4}W_{0.6}C_2T_z$ and $Ti_{1.6}W_{0.4}CT_z$, respectively.

3.5 Performance of the Ti_{1-x}-W_x MXenes as SIB anodes

Both the MXenes were tested as SIB anodes in two different electrolytes. For $Ti_{2.4}W_{0.6}C_2T_z$ in carbonate electrolyte, the measured reversible capacities are 60 mAh/g (@50mA/g), 55 mAh/g (@100 mA/g), 50 mAh/g (@200 mA/g), 44 mAh/g (@500 mA/g) and 30 mAh/g (@1000 mA/g) (Figure 7a). When the same MXene was tested in diglyme (DG) electrolyte, the capacity at lower currents was comparable but was higher (40 mAh/g (@1000 mA/g)) compared to the ones tested in carbonate electrolyte at higher currents (Figure 7b). This MXene shows a remarkable rate performance where nearly ~50-60% of capacity is retained even when the current is increased 20 times. Moreover, the capacity at lower currents is completely recovered even after subjecting the MXene to high currents as seen in Figure 7a, where the capacity at 50 mA/g current is the same before and after the rate performance measurements.

The results are even more impressive in the case of $Ti_{1.6}W_{0.4}CT_z$ MXene in carbonate electrolyte and the values are approximately double compared to the $Ti_{2.4}W_{0.6}C_2T_z$. The capacity measured was 112 mAh/g (@50mA/g), 105 mAh/g (@ 100 mA/g), 95 mAh/g (@200 mA/g), 83 mAh/g (@500 mA/g) and 70 mAh/g (@1000 mA/g) (Figure 7c). Similar values were obtained for the same MXene tested in DG-based electrolytes as well (Figure 7d). It is appreciable that the capacity value of 70 mAh/g obtained at a high current of 1000 mA/g in the case of $Ti_{1.6}W_{0.4}CT_z$ is still higher than the capacity of 60 mAh/g obtained at a small current of 50 mA/g for $Ti_{2.4}W_{0.6}C_2T_z$. In the rate performance measurements of $Ti_{1.6}W_{0.4}CT_z$, ~60% of the capacity is also maintained when the current is increased 20 times. In the case of carbonate electrolyte, the first cycle capacity is only ~100 mAh/g, which is significantly lower than other MXenes. Comparing the capacitance of various multilayered MXene Na-ion anodes in literature we find the performance of $Ti_{1.6}W_{0.4}CT_z$ is the best when comparing factors like capacity, rate performance, and first cycle capacity loss (Table S10).

The impact of the electrolytes on Coulombic efficiency (CE) is significant. With carbonate electrolytes, the CEs approach 100% after the initial cycles and remain stable thereafter. In contrast, when using DG electrolytes, the CE consistently decreases over cycles in both types of MXenes. This observation highlights a notable difference from graphite, where DG electrolytes typically outperform carbonate electrolytes. However, in the case of MXenes serving as electrodes for sodium-ion batteries, carbonate electrolytes demonstrate superior performance.

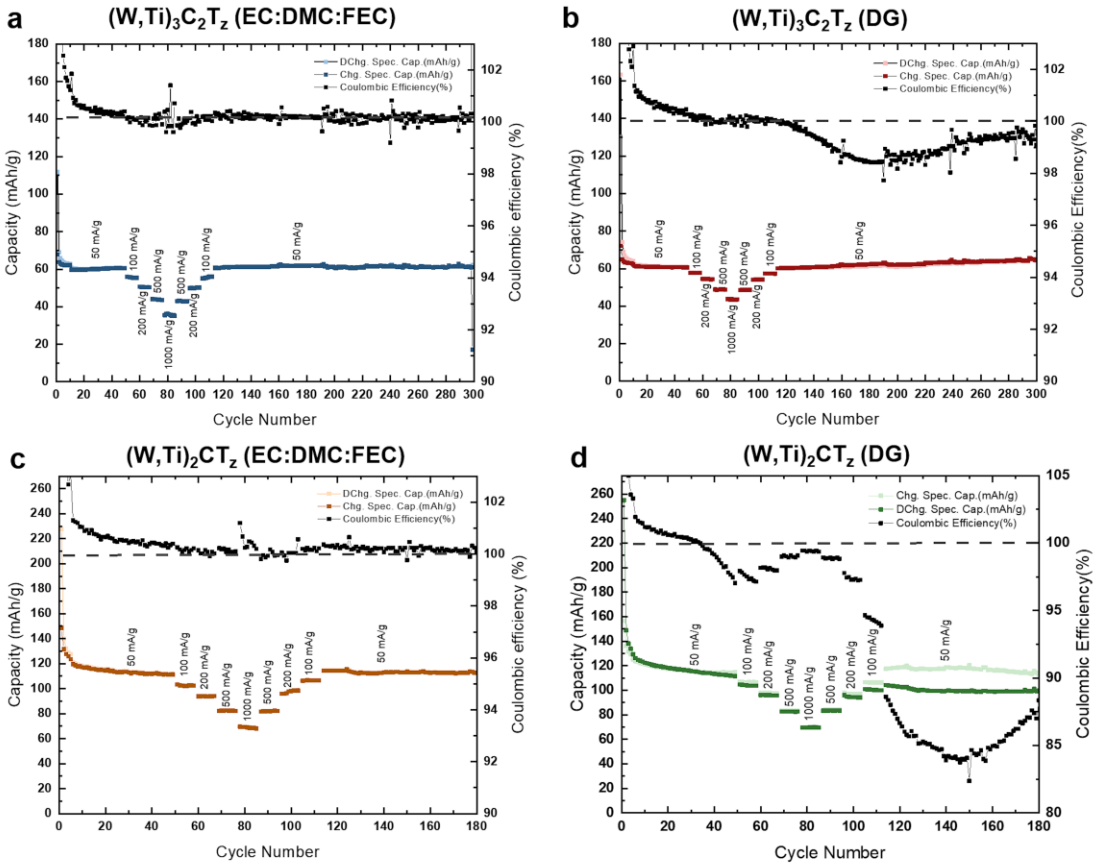

Figure 7. Cycling and Rate Performance of $Ti_{2.4}W_{0.6}C_2T_z$ in (a) carbonate and (b) glyme electrolyte, and of $Ti_{1.6}W_{0.4}CT_z$ in (c) carbonate and (d) glyme electrolyte.

Figure S18 represents the dQ/dV vs Voltage (V) curve which is plotted using charge-discharge curves plotted in Figure S19, these plots provide information about the sodium de-intercalation/intercalation between the MXene layers. In the dQ/dV plots desodiation and sodiation peaks are measured at 2.6, 0.8, 0.06 V irrespective of the MXene type or the electrolyte. This implies that the sodium ion storage mechanism is similar in all 4 cases. The 2.6V pair of peaks are the highest voltage redox reactions recorded in MXenes as per our knowledge. The exact redox reactions occurring around 0.8 V and 2.6 V need to be studied in detail using in-situ XRD and XAS, but this is out of the scope of this study. The low V peak around 0V is ascribed to the Na ion storage in the conducting carbon black used to make the battery electrodes and not to MXene.

4. Conclusions

New Ti_{1-x}-W_x double transition metal solid solution MAX phases were synthesized, including 211-type $Ti_{2-x}W_xAlC$ and 312-type $Ti_{3-x}W_xAlC_2$, with up to 40% W substituting for Ti. Detailed crystallographic analysis revealed that compositions with 10-20% W produced

highly pure targeted phases, while those with 30-40% W resulted in surplus phases including other MAX phases, a novel $Ti_{17.6}W_{8.4}$, metal carbides, and residual metals. Furthermore, the 312-structure exhibited a pronounced tendency to form o-MAX phases as W content increased. This distinct ordering is primarily attributed to the unique electronic structure and atomic radius of tungsten, factors that are crucial in stabilizing the outer planes of the 312-type MAX phase. The $Ti_{1.6}W_{0.4}AlC$ and $Ti_{2.4}W_{0.6}AlC_2$ phases, containing 20% W, served as precursors for synthesizing new W-containing solid solution MXenes in the forms of $Ti_{1.6}W_{0.4}CT_z$ and $Ti_{2.4}W_{0.6}C_2T_z$, both as multilayers and single flakes. These MXenes' optical, structural, and chemical properties were thoroughly assessed. Electrochemical testing of these MXenes as SIB anodes revealed that $Ti_{1.6}W_{0.4}CT_z$ performed significantly better than $Ti_{2.4}W_{0.6}C_2T_z$, achieving specific capacities of 112 and 70 mAh/g at current densities of 50 and 1000 mA/g, respectively, compared to 60 and 30 mAh/g for $Ti_{2.4}W_{0.6}C_2T_z$. This performance is among the highest reported for any multilayer MXene tested as SIB anodes, underscoring the potential of these materials in advanced energy storage applications.

Acknowledgements

This work was supported by the Israel Science Foundation (grant No. 2527/22).

Yugal Rathod and Varun Natu acknowledge CSIR-NCL startup grant for support.

The authors thank Guy Avrahami from Tel Aviv University for performing the UV-VIS measurements and Dr. Pini Shekhter from Tel Aviv University Center for Nanoscience and Nanotechnology for his assistance with the XPS measurements.

5. References

[1] M. Sokol, V. Natu, S. Kota, M. W. Barsoum, *Trends Chem.* **2019**, *1*, 210.

[2] M. Dahlqvist, M. W. Barsoum, J. Rosen, *Mater. Today* **2024**, *72*, 1.

[3] M. Radovic, M. W. Barsoum, *Am. Ceram. Soc. Bull.* **2013**, *92*, 20.

[4] M. W. Barsoum, *MAX Phases Properties of Machinable Ternary Carbides and Nitrides*, WILEY-VCH Verlag GmbH & Co. KGaA, **2013**.

[5] J. Gonzalez-Julian, *J. Am. Ceram. Soc.* **2021**, *104*, 659.

[6] Z. Zhang, X. Duan, D. Jia, Y. Zhou, S. van der Zwaag, *J. Eur. Ceram. Soc.* **2021**, *41*, 3851.

[7] K. R. G. Lim, M. Shekhirev, B. C. Wyatt, B. Anasori, Y. Gogotsi, Z. W. Seh, *Nat. Synth.* **2022**, *1*, 601.

[8] M. Downes, C. E. Shuck, B. McBride, J. Busa, Y. Gogotsi, *Nat. Protoc.* **2024**, 1.

[9] W. Hong, B. C. Wyatt, S. K. Nemani, B. Anasori, *MRS Bull.* **2020**, *45*, 850.

[10] J. Rosen, D. Martin, T. Quanzheng, L. Hultman, In *2D Metal Carbides and Nitrides (MXenes)* (Eds.: Anasori, B.; Gogotsi, Y.), Springer, **2019**, pp. 37–52.

[11] H. Ding, Y. Li, M. Li, K. Chen, K. Liang, G. Chen, J. Lu, J. Palisaitis, P. O. Å. Persson, P. Eklund, L. Hultman, S. Du, Z. Chai, Y. Gogotsi, Q. Huang, *Science (80-.).* **2023**, *379*, 1130.

[12] M. Han, K. Maleski, C. E. Shuck, Y. Yang, J. T. Glazar, A. C. Foucher, K. Hantanasirisakul, A. Sarycheva, N. C. Frey, S. J. May, V. B. Shenoy, E. A. Stach, Y. Gogotsi, *J. Am. Chem. Soc.* **2020**, *142*, 19110.

[13] S. K. Nemani, B. Zhang, B. C. Wyatt, Z. D. Hood, S. Manna, R. Khaledialidusti, W. Hong, M. G. Sternberg, S. K. R. S. Sankaranarayanan, B. Anasori, *ACS Nano* **2021**, *15*, 12815.

[14] J. Zhou, Q. Tao, B. Ahmed, J. Palisaitis, I. Persson, J. Halim, M. W. Barsoum, P. O. Å. Persson, J. Rosen, *Chem. Mater.* **2022**, *34*, 2098.

[15] F. L. Meng, Y. C. Zhou, J. Y. Wang, *Scr. Mater.* **2005**, *53*, 1369.

[16] C. Zuo, C. Zhong, *Mater. Chem. Phys.* **2020**, *250*, 123059.

[17] L. Wang, M. Han, C. E. Shuck, X. Wang, Y. Gogotsi, *Nano Energy* **2021**, *88*, 106308.

[18] I. M. Chirica, A. G. Mirea, Ş. Neaţu, M. Florea, M. W. Barsoum, F. Neaţu, *J. Mater. Chem. A* **2021**, *9*, 19589.

[19] P. Das, Z. S. Wu, *JPhys Energy* **2020**, *2*, 032004.

[20] D. Pinto, B. Anasori, H. Avireddy, C. E. Shuck, K. Hantanasirisakul, G. Deysher, J. R. Morante, W. Porzio, H. N. Alshareef, Y. Gogotsi, *J. Mater. Chem. A* **2020**, *8*, 8957.

[21] M. Pandey, K. Deshmukh, A. Raman, A. Asok, S. Appukuttan, G. R. Suman, *Renew.*

Sustain. Energy Rev. **2024**, *189*, 114030.

[22] X. Wang, X. Shen, Y. Gao, Z. Wang, R. Yu, L. Chen, *J. Am. Chem. Soc.* **2015**, *137*, 2715.

[23] S. Kajiyama, L. Szabova, K. Sodeyama, H. Iinuma, R. Morita, K. Gotoh, Y. Tateyama, M. Okubo, A. Yamada, *ACS Nano* **2016**, *10*, 3334.

[24] J. Zhu, M. Wang, M. Lyu, Y. Jiao, A. Du, B. Luo, I. Gentle, L. Wang, *ACS Appl. Nano Mater.* **2018**, *1*, 6854.

[25] K. Liang, A. Tabassum, A. Majed, C. Dun, F. Yang, J. Guo, K. Prenger, J. J. Urban, M. Naguib, *InfoMat* **2021**, *3*, 1422.

[26] Y. Wu, P. Nie, J. Jiang, B. Ding, H. Dou, X. Zhang, *ChemElectroChem* **2017**, *4*, 1560.

[27] S. Zhang, W. Q. Han, *Phys. Chem. Chem. Phys.* **2020**, *22*, 16482.

[28] Y. Zhang, Z. Feng, X. Wang, H. Hu, M. Wu, *Mater. Today Sustain.* **2023**, *22*, 100350.

[29] L. Lu, G. Guan, J. Wang, W. Meng, S. Li, Y. Zhang, F. Guo, *Chem. Eng. J.* **2024**, *480*, 147999.

[30] J. Y. Hwang, S. T. Myung, Y. K. Sun, *Chem. Soc. Rev.* **2017**, *46*, 3529.

[31] C. Vaalma, D. Buchholz, M. Weil, S. Passerini, *Nat. Rev. Mater.* **2018**, *3*, 18013.

[32] Q. Wang, X. Zhang, Z. Chen, Y. Zhao, W. Yao, J. Xu, *J. Alloys Compd.* **2023**, *954*, 170128.

[33] Z. He, L. Yao, W. Guo, N. Sun, F. Wang, Y. Wang, R. Wang, F. Wang, *Adv. Funct. Mater.* **2023**, *33*, 2305251.

[34] H. Zheng, J. Z. Ou, M. S. Strano, R. B. Kaner, A. Mitchell, K. Kalantar-Zadeh, *Adv. Funct. Mater.* **2011**, *21*, 2175.

[35] Y. Q. Sun, W. Fu, Y. X. Hu, J. Vaughan, L. Z. Wang, *Tungsten* **2021**, *3*, 245.

[36] M. Rafique, Q. Fu, J. Han, R. Wang, T. Yao, X. Wang, B. Song, *ChemElectroChem* **2024**, *11*, e202300722.

[37] R. Meshkian, M. Dahlqvist, J. Lu, B. Wickman, J. Halim, J. Thörnberg, Q. Tao, S. Li, S. Intikhab, J. Snyder, M. W. Barsoum, M. Yildizhan, J. Palisaitis, L. Hultman, P. O.

Å. Persson, J. Rosen, *Adv. Mater.* **2018**, *30*, 1706409.

[38] H. Weng, A. Ranjbar, Y. Liang, Z. Song, M. Khazaei, S. Yunoki, M. Arai, Y. Kawazoe, Z. Fang, X. Dai, *Phys. Rev. B - Condens. Matter Mater. Phys.* **2015**, *92*, 075436.

[39] R. K. Choudhury, B. R. Bhagat, K. H. Mali, R. Pokar, A. Dashora, *Appl. Surf. Sci.* **2022**, *603*, 154426.

[40] H. Pan, *Sci. Rep.* **2016**, *6*, 32531.

[41] S. Ke, X. Min, Y. Liu, R. Mi, X. Wu, Z. Huang, M. Fang, *Molecules* **2022**, *27*, 4751.

[42] U. Sohail, E. Pervaiz, M. Ali, R. Khosa, A. Shakoor, U. Abdullah, *FlatChem* **2022**, *35*, 100404.

[43] M. Zheng, H. Tang, Q. Hu, S. Zheng, L. Li, J. Xu, H. Pang, *Adv. Funct. Mater.* **2018**, *28*, 1707500.

[44] J. Huang, Z. Wei, J. Liao, W. Ni, C. Wang, J. Ma, *J. Energy Chem.* **2019**, *33*, 100.

[45] Y. Li, J. Qian, M. Zhang, S. Wang, Z. Wang, M. Li, Y. Bai, Q. An, H. Xu, F. Wu, L. Mai, C. Wu, *Adv. Mater.* **2020**, *32*, 2005802.

[46] J. Yang, R. Liu, N. Jia, K. Wu, X. Fu, Q. Wang, W. Cui, *Carbon N. Y.* **2021**, *183*, 76.

[47] Z. Chen, H. Chong, S. Sun, J. Yang, G. Yao, Q. Wang, J. Zhu, S. Yang, W. Cui, *Scr. Mater.* **2022**, *213*, 114596.

[48] P. Cai, Q. He, L. Wang, X. Liu, J. Yin, Y. Liu, Y. Huang, Z. Huang, *Ceram. Int.* **2019**, *45*, 5761.

[49] L. Wang, Q. Chen, T. Yang, B. Guo, Y. Cheng, W. Xu, *J. Mater. Sci. Mater. Electron.* **2022**, *33*, 17446.

[50] M. Alhabeb, K. Maleski, T. S. Mathis, A. Sarycheva, C. B. Hatter, S. Uzun, A. Levitt, Y. Gogotsi, *Angew. Chemie - Int. Ed.* **2018**, *57*, 5444.

[51] B. Anasori, J. Lu, O. Rivin, M. Dahlqvist, J. Halim, C. Voigt, J. Rosen, L. Hultman, M. W. Barsoum, E. N. Caspi, *Inorg. Chem.* **2019**, *58*, 1100.

[52] B. H. Toby, R. B. Von Dreele, *J. Appl. Crystallogr.* **2013**, *46*, 544.

[53] O. V. Dolomanov, L. J. Bourhis, R. J. Gildea, J. A. K. Howard, H. Puschmann, *J. Appl. Crystallogr.* **2009**, *42*, 339.

[54] S. Thimmaiah, G. J. Miller, *Inorg. Chem.* **2013**, *52*, 1328−1337.

[55] M. Dahlqvist, J. Rosen, *Phys. Chem. Chem. Phys.* **2015**, *17*, 31810.

[56] E. N. Caspi, P. Chartier, F. Porcher, F. Damay, T. Cabioc'h, *Mater. Res. Lett.* **2015**, *3*, 100.

[57] M. T. P. Rigby, V. Natu, M. Sokol, D. J. Kelly, D. G. Hopkinson, Y. Zou, J. R. T. Bird, L. J. Evitts, M. Smith, C. P. Race, P. Frankel, S. J. Haigh, M. W. Barsoum, *RSC Adv.* **2021**, *11*, 3110.

[58] B. Anasori, M. Dahlqvist, J. Halim, E. J. Moon, J. Lu, B. C. Hosler, E. N. Caspi, S. J. May, L. Hultman, P. Eklund, J. Rosén, M. W. Barsoum, *J. Appl. Phys.* **2015**, *118*, 094304.

[59] Z. Liu, E. Wu, J. Wang, Y. Qian, H. Xiang, X. Li, Q. Jin, G. Sun, X. Chen, J. Wang, M. Li, *Acta Mater.* **2014**, *73*, 186.

[60] P. P. Michałowski, M. Anayee, T. S. Mathis, S. Kozdra, A. Wójcik, K. Hantanasirisakul, I. Jóźwik, A. Piątkowska, M. Możdżonek, A. Malinowska, R. Diduszko, E. Wierzbicka, Y. Gogotsi, *Nat. Nanotechnol.* **2022**, *17*, 1192.

[61] C. H. Suresh, N. Koga, *J. Phys. Chem. A* **2001**, *105*, 5940.

[62] J. C. Schuster, H. Nowotny, C. Vaccaro, *J. Solid State Chem.* **1980**, *32*, 213.

[63] M. Naguib, G. W. Bentzel, J. Shah, J. Halim, E. N. Caspi, J. Lu, L. Hultman, M. W. Barsoum, *Mater. Res. Lett.* **2014**, *2*, 233.

[64] M. Seitz, A. G. Oliver, K. N. Raymond, *J. Am. Chem. Soc.* **2007**, *129*, 11153.

[65] D. V. Suetin, I. R. Shein, A. L. Ivanovskii, *J. Phys. Chem. Solids* **2009**, *70*, 64.

[66] P. A. Burr, D. Horlait, W. E. Lee, *Mater. Res. Lett.* **2017**, *5*, 144.

[67] M. Naguib, R. R. Unocic, B. L. Armstrong, J. Nanda, *Dalt. Trans.* **2015**, *44*, 9353.

[68] H. Kim, B. Anasori, Y. Gogotsi, H. N. Alshareef, *Chem. Mater.* **2017**, *29*, 6472.

[69] X. Sang, Y. Xie, M. W. Lin, M. Alhabeb, K. L. Van Aken, Y. Gogotsi, P. R. C. Kent,

K. Xiao, R. R. Unocic, *ACS Nano* **2016**, *10*, 9193.

[70] K. Maleski, C. E. Shuck, A. T. Fafarman, Y. Gogotsi, *Adv. Opt. Mater.* **2021**, *9*, 2001563.

[71] K. Shevchuk, A. Sarycheva, C. E. Shuck, Y. Gogotsi, *Chem. Mater.* **2023**, *35*, 8239.

[72] S. Huang, V. N. Mochalin, *Inorg. Chem.* **2019**, *58*, 1958.

[73] P. Hou, Y. Tian, Y. Xie, F. Du, G. Chen, A. Vojvodic, J. Wu, X. Meng, *Angew. Chemie* **2023**, *135*, e202304205.

[74] B. Favelukis, S. Chakrabartty, V. Kumar, S. H. Kim, A. El-Zoka, M. Krämer, D. Raabe, B. Gault, N. Eliaz, A. Natan, M. Sokol, B. A. Rosen, *Adv. Funct. Mater.* **2024**, *34*, 2309749.